



Calcium sulfate-based load-bearing bone grafts with patient-specific geometry

Seyed Alireza Mirmohammadi^a, Damiano Pasini^a, Francois Barthelat^{b,*}

^a Department of Mechanical Engineering, McGill University, Montreal, Quebec, Canada

^b Department of Mechanical Engineering, University of Colorado, Boulder, CO, USA

ABSTRACT

The treatment of bone defects with complex three-dimensional geometry presents challenges in terms of bone grafting and restoration. In this paper, we propose a rapid and effective method that uses 3D printing, ceramic casting, and the incorporation of mesh reinforcement to create load-bearing bone grafts with patient-specific three-dimensional geometry. Using two types of facial bones as examples, we show that this fabrication method has a high degree of geometrical fidelity. We also experimentally study the fracture behavior of six different architectures designed for the treatment of mandibular defects, one of the principal load-bearing facial bones. These design configurations include un-reinforced calcium sulfate samples, and samples reinforced with one or two layers of stainless steel, poly (lactic acid), and poly (L-lactic acid). The results suggested a trade-off between energy dissipation and maximum load based on the position of the metal mesh in the sample. Samples reinforced with one layer of metallic mesh at their lowermost margin exhibited a 17% higher stiffness and a 21.3% higher peak load, while samples with a layer of metal mesh embedded within dissipated 16% more energy. Samples with two layers of metallic mesh demonstrated the highest improvements among all samples, dissipating 5767.85% more energy and exhibiting a peak load 145.6% higher compared to plain CS. The improvements in stiffness for SD, SL, and S2 were 3%, 21.3%, and 21.9% respectively compared to the plain ceramic. In contrast, PLA mesh improved energy dissipation by 96.71% but reduced the peak load by 29.18%, while PLLA mesh decreased both the peak load and the dissipated energy by 13.05% and 35.31%, respectively. While PLA mesh reduced stiffness by 11% compared to plain CS, PLLA mesh-reinforced samples were slightly stiffer than pure CS by 1.6%.

1. Introduction

Large segmental bone defects do not heal without external treatment (Tennyson et al., 2021), and they remain a significant challenge in orthopedic and reconstructive surgery. Notably, intricate three-dimensional geometrical features in the cranio-maxillofacial regions make reconstructive surgery extremely difficult, since both aesthetic and performance considerations are required for reconstruction from trauma, tumor resection, or congenital abnormalities (Rudman et al., 2011).

From a functional standpoint, the ideal bone graft material should satisfy three main requirements: i) biocompatibility and stimulation of bone formation; ii) mechanical performance comparable to that of natural bone (stiffness, strength, and toughness); iii) bioresorption to avoid fatigue failure over the long term (Bohner et al., 2012; Cavalier et al., 2021). Although autografts are currently considered the most effective method for treating segmental bone defects, there are drawbacks related to the availability of viable bone tissue, tissue damage, morbidity, and persistent pain at the donor site (Lethaus et al., 2014; Wang and Yeung, 2017). Synthetic bone grafts made of biomaterials

such as polymers, titanium, and bioceramics provide a promising alternative for treating bone defects (Wang and Yeung, 2017). However, titanium is not resorbable, and polymers suffer from structural integrity (Cavelier et al., 2021). The degradation of hydroxyapatite (HA) takes years in the body and calcium phosphate does not offer adequate mechanical properties without sintering (Cavelier et al., 2021; Goel et al., 2013). Calcium sulfate (CS) possesses attractive properties, making it a potential candidate for producing an ideal bone graft material. CS is a biocompatible, fully biodegradable (Thomas and Puleo, 2009; Pietrzak and Ronk, 2000), and osteoconductive (Pietrzak and Ronk, 2000; Moore et al., 2001) ceramic that can trigger the ingrowth of blood vessels and stem cells (Moore et al., 2001). Although CS does not possess adequate strength and toughness, its preparation method can be optimized to maximize its strength (Cavelier et al., 2020). However, the mechanical properties of CS, particularly its toughness, are still far from that of natural bone (Cavelier et al., 2021).

The attractive combination of stiffness, strength, and toughness in natural bone can be associated with its hierarchical structure, which activates different toughening mechanisms at several levels of the hierarchy (Launey et al., 2010; Barthelat et al., 2016; Zhang et al., 2011).

* Corresponding author.

E-mail address: francois.barthelat@colorado.edu (F. Barthelat).

Crack deflection along the interfaces at multiple levels of the hierarchy (Cavelier et al., 2021), combined with other features such as adhesive properties (Cavelier et al., 2018), leads to the high toughness of bone. Some of these mechanisms can be duplicated in synthetic materials. For example, incorporating weak interfaces in multilayered materials has been exploited to design layered ceramics with high toughness (Barthelat, 2015; Clegg et al., 1990). Incorporating a second phase as reinforcement is another strategy used to overcome the inherently low fracture resistance of brittle materials. Reinforcements can activate toughening mechanisms such as crack bridging and deflection (Rühle and Evans, 1989; Tuan and Chen, 2002; Campbell et al., 1990). In the case of brittle reinforcements, if fiber fracture is prevented at the crack front, the composite can exhibit high toughness (Evans et al., 1989). Intact ligaments contribute to the toughness by the traction they exert on the crack face, while broken ligaments' contribution arises from their frictional sliding along the debonded surface during pull-out (Thouless and Evans, 1988). Ductile reinforcement also contributes to the overall toughness through plastic deformation (Evans, 1990). Various geometries for the reinforcements are possible, including fibers (Zok and Hom, 1990; Yang and Tieg, 1995; Topoleski et al., 1992), whiskers (Campbell et al., 1990), particles (Krstic, 1983), layers (Chen and Mecholsky, 1993) and meshes (Cavelier et al., 2021; Weir et al., 2006; Xu and Simon, 2004; Xu et al., 2004). Among different forms of reinforcements, textile or patterned fibers offer adequate control over the architecture of the final composite by initiating toughening mechanisms operating in fiber-reinforced materials; this in turn allows for the precise adjustment of the mechanical properties (Cavelier et al., 2021). Successful reinforcement of ceramics with meshes to produce bone graft materials has also been explored (Weir et al., 2006; Xu and Simon, 2004; Xu et al., 2004). Indeed, we recently reported improvements in the strength and toughness of CS by incorporating titanium meshes into this ceramic (Cavelier et al., 2021).

Although bone graft materials with adequate functional characteristics have been developed, these bone grafts fall short in terms of aesthetics. In this context, patient-specific methods have emerged as promising techniques for treating large complex-shaped bone defects (Rudman et al., 2011; Falkhausen et al., 2021). Due to the control 3D printing offers over the size, porosity, shape, and structure, this fabrication method has been extensively used in orthopedic (Masaeli et al., 2019) to produce customized implants such as titanium implants with desired porosity (Abar et al., 2022; Bachelet et al., 2018; Arabnejad et al., 2017; Dérand et al., 2012), polymeric implants (Honigmann et al., 2018; Ivanovski et al., 2024), and bioceramic scaffolds (Kim et al., 2024; Zhang et al., 2022; Tesavibul et al., 2012; Klammert et al., 2010). In particular, bioceramics have attracted considerable attention due to their potential to replicate the properties of natural bone (Thangavel and ElsenSelvam, 2022; Ma et al., 2018). Thus, many studies have focused on improving the mechanical properties of 3D printed bioceramics. For instance, researchers have 3D printed glass scaffolds as strong as cortical bone (in compression) (Fu et al., 2011; Deliormanli and Rahaman, 2012). Mg-doped Baghdadite scaffolds with stiffness and strength comparable to that of cortical bone have also been 3D printed (Mirkhalaf et al., 2021a). Other materials such as hydroxyapatite have also been used to 3D print bone substitutes with a bending strength of 92.4 MPa (Yao et al., 2021). While these materials offer high strength and stiffness, they continue to suffer from low fracture resistance and poor reliability (Mirkhalaf et al., 2021b). Additionally, they require additional post-processing steps such as sintering at elevated temperatures (Thangavel and ElsenSelvam, 2022; Ma et al., 2018), which can be costly and time-consuming. Adding biological molecules to ceramic scaffolds that require sintering is also complicated (Laurencin et al., 2014). Furthermore, 3D printing methods that can produce bone graft materials with high performance require costly equipment, underscoring the need for interdisciplinary approaches to create affordable bone graft materials (Ma et al., 2018).

Indirect 3D printing is a related approach that offers major

advantages over direct 3D printing: material versatility (Wang et al., 2019; Sapkal et al., 2017; Schumacher et al., 2010; Van Damme et al., 2020), as a wider range of materials not necessarily biocompatible, can be used in the 3D printing of the mold. Indirect 3D printing also allows for the production of cost-effective materials with high geometric fidelity, eliminates the need for toxic and pollutant materials as binders or photo absorbers, enables efficient material use, and alleviates the need for the preprocessing of the raw materials (Du et al., 2024; Esslinger and Gadow, 2020; Jain et al., 2021). A study comparing the properties of hydrogel scaffolds manufactured through direct and indirect 3D printing demonstrated that similar properties can be attained, regardless of the technique. It concluded that indirect 3D printing can overcome the shortcomings of direct 3D printing (Van Damme et al., 2020).

Currently, there is no affordable patient-specific bone graft that can fully meet all the requirements of an ideal bone graft material. The existing bone grafts usually lack several qualities including affordability, customizability, strength, stiffness, toughness, biocompatibility, or biodegradability. Calcium sulfate is a good candidate for bone grafts (Cavelier et al., 2020, 2021), but 3D printed CS scaffolds (Asadi-Eydivand et al., 2016; Qi et al., 2017; Hamano et al., 2021; Ansari et al., 2023) lack the necessary mechanical properties for load-bearing applications due to defects formed in their structures during the manufacturing process. Given the attractive properties of CS and limitations of existing 3D printed ceramic scaffolds, this study seeks to produce patient-specific CS bone grafts for load-bearing applications. In particular, we rely on the hypothesis that the previous strategies we developed to enhance CS properties (Cavelier et al., 2020, 2021) can be integrated with 3D printing to produce affordable patient-specific multilayered bone graft materials that can combine stiffness, strength, toughness, degradation, and biocompatibility. We demonstrate that our method allows for a high level of control over material choice, size, and arrangement of components, thereby enabling biomedical engineers to design affordable bone graft materials with a broad spectrum of properties.

2. Overview of the bone grafts

The main objective of this study is to develop a rapid and inexpensive method to fabricate patient-specific bone graft materials with mechanical performance and physical properties similar to those of natural bone. As geometrical models, we considered three facial regions: i) the lateral orbital rim and ii) the orbital floor due to their very complex geometries; iii) the mandible body as it is one of the main load-bearing facial bones (Fig. 1). We used the orbital bones to assess the geometric fidelity of our method due to their highly complex geometries, and we did not test their mechanical properties. We tested only the mechanical properties of the mandible body. Mandible fracture is one of the most common fractures among facial bones in maxillofacial trauma (Afrooz et al., 2015). The shape and structure of the mandible have evolved to sustain large physiological stresses during mastication and biting, most notably from shear and bending loads in the sagittal plane. For this reason, denser cortical bone is found on the upper and lower margins where high tensile and compressive stresses occur, and the lower parts of the mandible body and symphysis are thicker than their upper parts, providing the mandible with higher resistance against tensile stresses (van Eijden, 2000; Wong et al., 2010).

CS shares a characteristic with natural bone and other brittle materials: it is prone to crack propagation under tensile loads, while it is stronger in compression (van Eijden, 2000). Inspired by the architecture of the mandible, in this study, we explore several strategies to enhance the performance of CS. Each of them is characterized by a specific design that varies the reinforcement material and arrangement of components. For the type of mesh reinforcement, we considered: a metallic mesh (stainless steel) and two polymeric meshes (polylactic acid, PLA and poly L-lactic acid, PLLA). Polylactic acids, primarily found in nature in the form of L-lactide (PLLA), are a group of biodegradable and

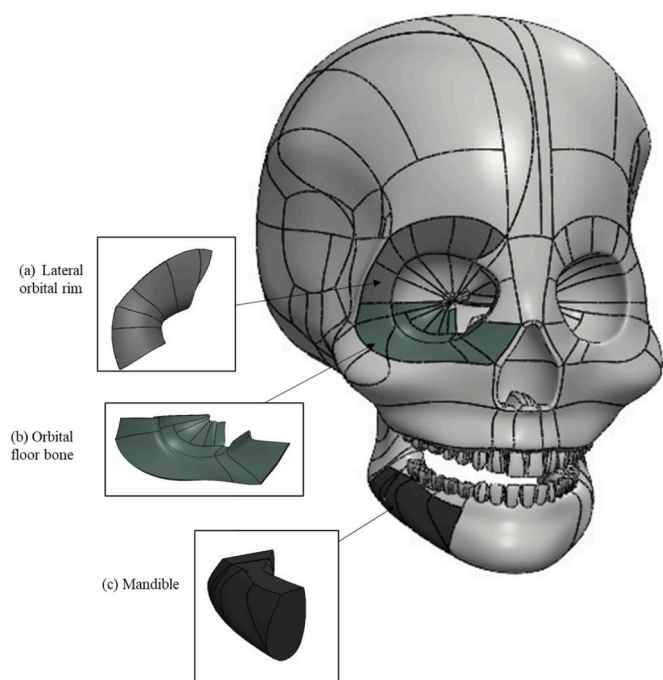


Fig. 1. Computer-aided design of the human skull (GrabCAD, 2018) and the 3D models used to 3D print the replicas: (a) lateral orbital rim bone, (b) orbital floor bone, and (c) mandible.

biocompatible polymers (Canal and Ginebra, 2011). These polymers have a variety of applications in medicine (DeStefano et al., 2020) in the form of PLA fibers (Petre et al., 2019), additives (Hasan et al., 2014), braids (Chen et al., 2017) as well as PLLA fibers (Zuo et al., 2010; Mulky et al., 2014; Castro et al., 2017; Thomas, 2013). In a separate study (Mirmohammadi et al.), we showed that a PLLA coating can decrease the dissolution rate of CS. For this reason, PLLA and PLA were selected as reinforcement materials in this study. For the arrangement of the components, we considered six design configurations: type (i) samples made of plain CS, denoted as P; types (ii-iv) samples, respectively, with one layer of stainless steel, PLLA, and PLA mesh at the lowermost border, here identified as SL, PLLA, and PLA. We also examined a type (v) sample, namely SD, with one layer of metallic mesh embedded in the

main body of the sample, three mm from the lowermost face of the samples. Finally, the last group of samples, type (vi), referred to as S2, was reinforced with two layers of metallic mesh, one at the lowermost face and the other three mm from the lowermost face.

3. Fabrication protocol

In this study, we used an indirect 3D printing strategy. While a detailed, three-dimensional anatomy of a bone injury can be obtained from a CT scan using commercially available software, we did not pursue this path in this study. Rather we directly used a CAD model of a human skull available from open libraries (GrabCAD, 2018) to escape any potential for ethical issues (Fig. 1). We then isolated a selected subset from this 3D model of the skull and converted it into an STL format for 3D printing using SolidWorks (Dassault Systèmes, Fig. 2a). Next, we fabricated physical replicas of these geometries using fused deposition modeling (QIDI, i-fast, China/Ultimaker B.V., ED Utrecht, Netherland), using PLA as base material (Fig. 2b).

In the following step, the 3D printed replica was used as a template to create the negative molds: each template and silicone were placed in a container, which was sealed by a plate. We allowed the silicone to cure for about 1 h. Fig. 2c and d illustrate that this process created negative molds that replicated the exact geometry of the selected original facial bones. Once the molds were ready, we proceeded to prepare the reinforcements. Stainless steel mesh with a wire diameter of 0.35 mm and an open size of 0.71 mm was acquired from McMaster-Carr (USA). We 3D printed a PLA mesh replicating the architecture of the metallic mesh. A laser cutter was used to create a mesh from a PLLA film (Delta Scientific, CA) with a thickness of 0.05 mm. Fig. 3 shows the layout of the three meshes.

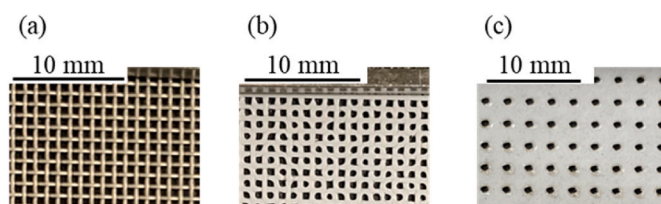


Fig. 3. Layout architecture of (a) metallic mesh; (b) PLA mesh and (c) PLLA mesh.

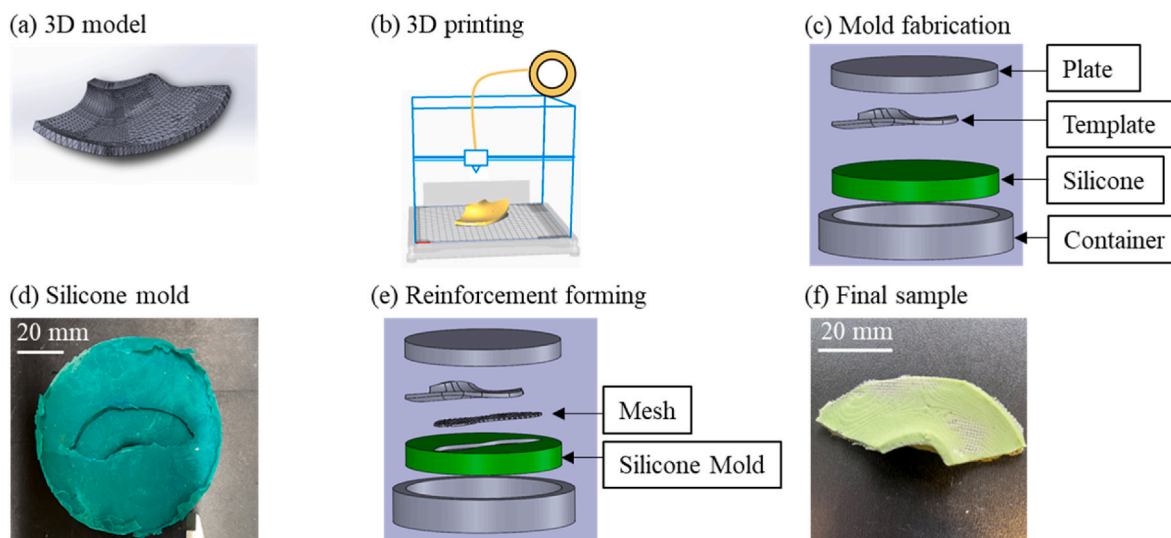


Fig. 2. Schematic representation of the fabrication protocol: (a) 3D model of a subset of the skull, converted to an STL file; (b) 3D printing of replica; (c) mold generation using 3D printed template and silicone; (d) silicone mold; (e) formation of stainless-steel mesh into the shape of the mold; (f) final sample reinforced with stainless-steel mesh.

To reinforce the patient-specific bone graft materials, we first needed to form the reinforcements into the shape of the final bone graft material. For this purpose, we projected the outline of the replica onto the mesh sheet by placing the replica on the mesh and tracing around its outline. Once we obtained the projection on the mesh, we cut the mesh along the outline and placed it on the silicone mold. Finally, we used the 3D-printed replica as a template to force and deform the metal mesh into the mold cavity using the press so as to enable the mesh to conform to the shape of the replica (Fig. 2e).

Unlike the metallic mesh, PLLA and PLA are not malleable. Therefore, forming required an additional step of heating the meshes above their glass transition temperature. This could be achieved by simply pouring hot water on the mold cavity after placing the mesh and before compression. As the meshes cooled, they recovered their rigidity and conformed to the shape of the cavity.

Once the meshes had the desired shapes, we prepared the CS matrix. The optimized method presented in the work by Cavelier et al. (2020) was here followed to fabricate the samples. We vigorously mixed the CS hemihydrate type V powder (Suprastone, Kerr Dental, Charlotte, NC) with water (10g:1.86g) until a homogenous paste was produced. We then poured the paste, together with the reinforcement, into the mold cavities. A piece of paper was used to absorb the excessive water. The silicone molds were then compressed using a hydraulic press to minimize porosity. The reaction of CS hemihydrate with water resulted in the full solidification of the sample in 2 h, after which we extracted it from the mold (Fig. 2f). The samples were left for 24 h at room temperature before performing the mechanical tests to ensure they reached their maximum strength (Pietrzak and Ronk, 2000).

4. Geometric fidelity

The lack of accuracy in the geometry of the implant can adversely affect aesthetic and functional performance, leading to intraoperative and postoperative complications (Smith et al., 2023). To assess the geometric fidelity of our bone grafts, we used a 3D scanner to quantitatively compare the shape of the physical bone grafts with the original 3D models. We aligned these 3D models with the original CAD models and assessed the geometry deviations using the cloud-to-mesh algorithm

available in CloudCompare (cloudcompare.org). We compared the lateral orbital rim and orbital floor samples with their original 3D models since these geometries were more complicated than that of the mandible.

Fig. 4 shows both quantitative and qualitative comparisons between the 3D models of the samples and the original 3D models visualized using a histogram and a color map. In the histograms, green represents high accuracy with small deviations, while blue and red indicate larger deviations from the original model. The histograms show that most of the points were in the green zone, indicating high accuracy. The quantitative analysis showed mean deviations of -0.11 and 0.32 mm, respectively, for the lateral orbital rim and orbital floor bone graft materials. The deviations of the manufactured samples from the original models can be attributed to the manufacturing process as well as the errors and inaccuracies of the 3D printing, scanning, and materials (Paré et al., 2022). For example, the edge of the sample grabbed by the holder during the scanning could not be captured in the 3D model of the casted samples, leading to an increase in the deviations. Other inaccuracies can be reduced by using 3D printers with higher resolution and silicone with higher quality to make the molds. Nevertheless, compared to typical values reported in the literature (Dienel et al., 2022; Moiduddin et al., 2023), the results show adequate accuracy of the method to capture complex geometries.

5. Mechanical performance

Since the mandible is one of the main load-bearing facial bones and is among the most commonly fractured due to trauma (Afrooz et al., 2015), this study focuses on the mechanical performance of the bone graft materials replicating the shape of the mandible body. The mandible is subjected to a combination of mechanical loads, including compression, shear, tension, bending, and torsion (van Eijden, 2000; Wong et al., 2010). The mandible has evolved in such a way as to show higher resistance against relatively large bending and vertical shear loads in the sagittal plane (van Eijden, 2000). Thus, in this study, we performed flexural tests, following several studies on the mechanical performance of bone graft materials (Shao et al., 2018; Hu et al., 2019; Yuan et al., 2007; Yang et al., 2014).

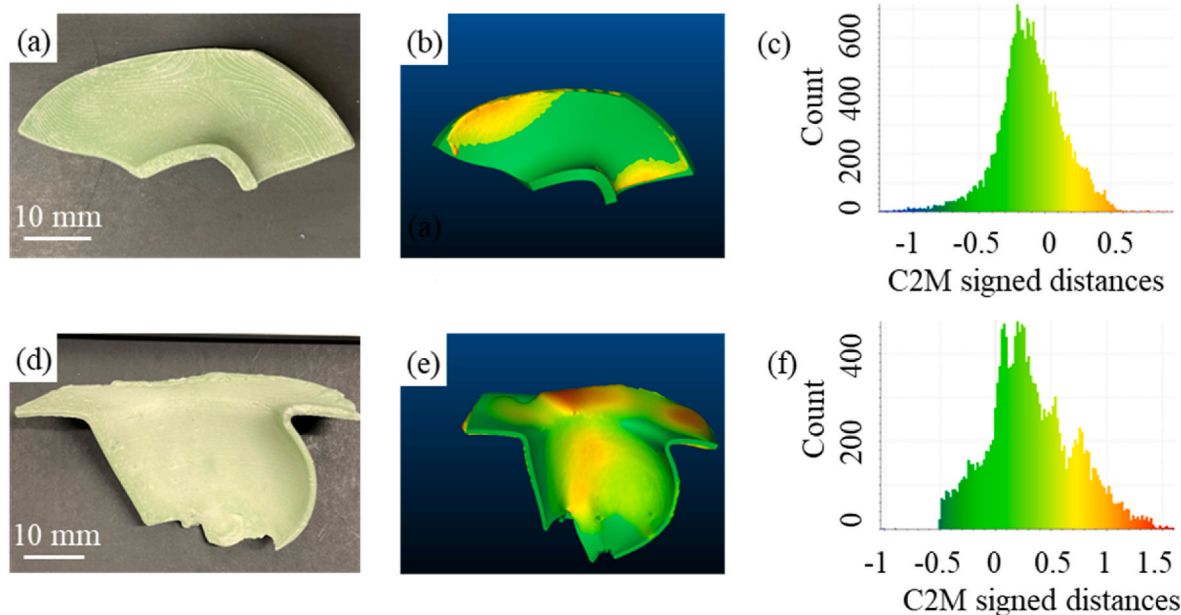


Fig. 4. (a) A lateral orbital rim bone graft; (b) comparison between the 3D model of the lateral orbital rim bone graft and the original 3D model, Color map indicates geometric accuracy with green being the highest and red the lowest; (c) histogram showing deviations of the CS graft from the CAD model (C2M: cloud to mesh, count: number of points that have a certain distance); (d) An orbital floor bone graft; (e) comparison between the 3D model of the orbital floor bone graft material and the original 3D model; (f) histogram showing deviations of the CS graft from the CAD model.

We performed three-point bending tests (Expert 5000, ADMET, Norwood, MA) with a span of 30 mm and at a quasi-static loading rate of 0.01 mm/s. We tested three samples for each configuration. The volume fraction of the reinforcement, φ , was determined using $\varphi = \frac{(100-OA)t_r A_r}{V}$, where OA is the open area, defined as the total surface of openings divided by the total surface area of the mesh, t_r , A_r , and V represent the reinforcement thickness, area, and the sample volume respectively. The reinforcement volume fraction was 1.8% for SD, SL, and PLA, while for S2 and PLLA, the volume fractions were 3.6% and 0.4%, respectively.

To obtain the stress distribution within the sample with complex and patient-specific geometry, a common approach is to rely on the finite element method, as the type and distribution of the internal stresses are strongly governed by the specific geometry. Here, however, our objective was to evaluate the mechanical integrity of the graft materials with sophisticated shapes rather than a simple beam. We thus decided to pursue mechanical testing of fabricated samples and characterize their force-displacement curves. Consequently, we reported here only forces and displacements, which we used for comparative assessment between grafts with identical geometry but dissimilar in material compositions and mesh layout. Fig. 5 shows a representative set of force-displacement curves for comparative assessment between the grafts. All samples showed a linear elastic region, and depending on the volume fraction of the reinforcement, its stiffness, and its position in the matrix, the samples showed different first cracking forces, marked by the first relative maximum, which was in this order: S2 > SL > SD > P > PLLA > PLA.

With the increase in the load, the matrix cracked at its extreme tensile fiber where the stress exceeded its tensile strength (McCormac and Brown, 2015). After the onset of cracks in the matrix, the multilayered bone graft materials showed dissimilar responses depending on the design. Samples reinforced with the metal mesh withstood higher loads after the first load drops while the samples reinforced with polymeric mesh either showed a catastrophic fracture (PLLA) or withstood a smaller load than the first peak (PLA). To simplify the post-fracture behavior analysis of the samples, we included snapshots of the samples during the flexural test (Fig. 6).

Plain CS is a brittle material, so the unstable propagation of a flexural crack in the vertical direction in CS led to a catastrophic fracture of the sample. However, full catastrophic failure was prevented by the metallic mesh which hindered crack propagation. The formation of each crack in the sample was characterized by a sudden drop in the applied force (Carmona et al., 2007). While crack propagation caused load drops, toughening mechanisms including crack bridging, crack deflection, and multiple cracking, activated by the metallic reinforcements, enabled the samples to continue carrying non-negligible forces even after crack propagation. Fig. 6 shows how the first crack initiated in these multilayers was perpendicular to the lowermost face of the samples. This flexural crack formed approximately in the mid-span at the lowermost fiber of the matrix, where the largest tensile stresses occurred. Due to the high thickness-to-span ratio (~ 0.5), significant shear stresses were

present in all samples. Although there were contributions from all three crack propagation modes due to the complex geometry, the crack propagated toward the loading nose under dominant mode I loading conditions in the SL and SD matrices and under mixed-mode I and II loading conditions (flexure-shear) in the S2 matrix. With the increase in the external load, all three types of samples showed the formation of additional cracks closer to the supports. The number of these cracks in S2, however, was greater than in the other two samples. These cracks were formed mainly due to shear (Demir et al., 2019). The onset and unstable growth of these cracks in SL, led to an abrupt failure of the sample, marked by the sharp load drop in the load-deflection curve. However, these cracks were effectively bridged and deflected into the interface between the matrix and reinforcement in SD and S2, leading to a gradual failure of the samples. These cracks propagated towards the loading nose, creating high stress concentrations on the compression side. Furthermore, the high stiffness of metallic mesh enabled the samples to withstand large tensile forces on the tensile side, leading to high compressive stresses under the loading nose (Abed et al., 2012). Consequently, the ceramic fractured in this area. Therefore, metallic mesh-reinforced samples failed due to a combination of flexural, shear, and compression failures.

Since cracks form in CS when the tensile stresses exceed its tensile strength, cracks usually grow perpendicular to the trajectories of principal tensile stresses (MacGregor et al., 1997). Fig. 7 illustrates the approximate trajectories of the principal tensile stresses under three-point bending. They are caused by a combination of bending and shear stresses in the tension part of the beam, and sole shear stresses at the neutral axis. The cracks in the metallic mesh-reinforced samples extended approximately perpendicular to the trajectories of principal tensile stresses toward the loading nose. However, this relationship is not always consistent because the onset of other cracks preceding the initiation of these shear-tension cracks causes a major stress redistribution which can alter the crack pattern (MacGregor et al., 1997).

As Fig. 5 shows, the S2 multilayer graft produced the highest area under the load-displacement curve (p values < 0.05) and peak load (p values < 0.05). The reason for the superior mechanical performance of S2 in comparison to SD and SL was twofold: first, these samples contained a higher volume fraction of metallic reinforcement than SD and SL, and once the brittle matrix cracked, the load was carried by the reinforcements (Xiao and Abbaschian, 1992). Since the metal had higher stiffness than CS (18.58 GPa (Cavelier et al., 2021)), S2 samples had higher resistance against tensile stresses compared to SL and SD. Higher volume fractions of metallic reinforcements also promoted multiple cracking, which enhanced energy dissipation (Howard et al., 1998; Shaw et al., 1993). Secondly, both numerical and experimental results showed that, for a given reinforcement volume fraction, increasing the number of layers resulted in greater energy dissipation (Cavelier et al., 2021; Mirmohammadi et al., 2022). The S2 samples were made of a higher number of layers (interfaces), which provided more paths for crack deflection, multiple crack formation, crack bridging, and energy dissipation through plastic deformation during the bending process (Cavelier et al., 2021; Wang et al., 2021; Sayyad and Patankar, 2013). These mesh layers bridged both flexural and shear cracks more effectively, leading to a higher number of cracks in S2. A more effective operation of the toughening mechanisms described above led to several relative maximum loads and higher displacement to failure in the load-displacement curve.

While multiple cracks formed and propagated in the matrices of the metal-reinforced samples, the failure of PLLA and PLA was due to the propagation of only one dominant crack. In PLA, a vertical crack developed first in the matrix in the region with high tensile stresses. The vertical crack then turned into a flexure-shear crack, which extended under dominant mixed-mode I and II loading conditions up to the loading nose. Although the PLA mesh was able to bridge the crack, due to the low stiffness of the reinforcement, the load drop for PLA was sharp, and these samples did not exhibit any second peak load higher

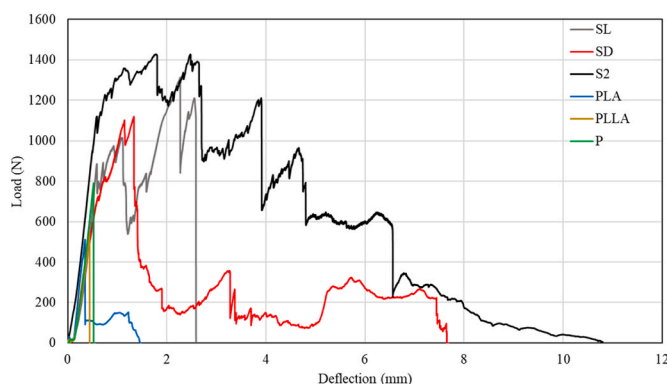


Fig. 5. Load-deflection curves for the mandibular bone graft materials.

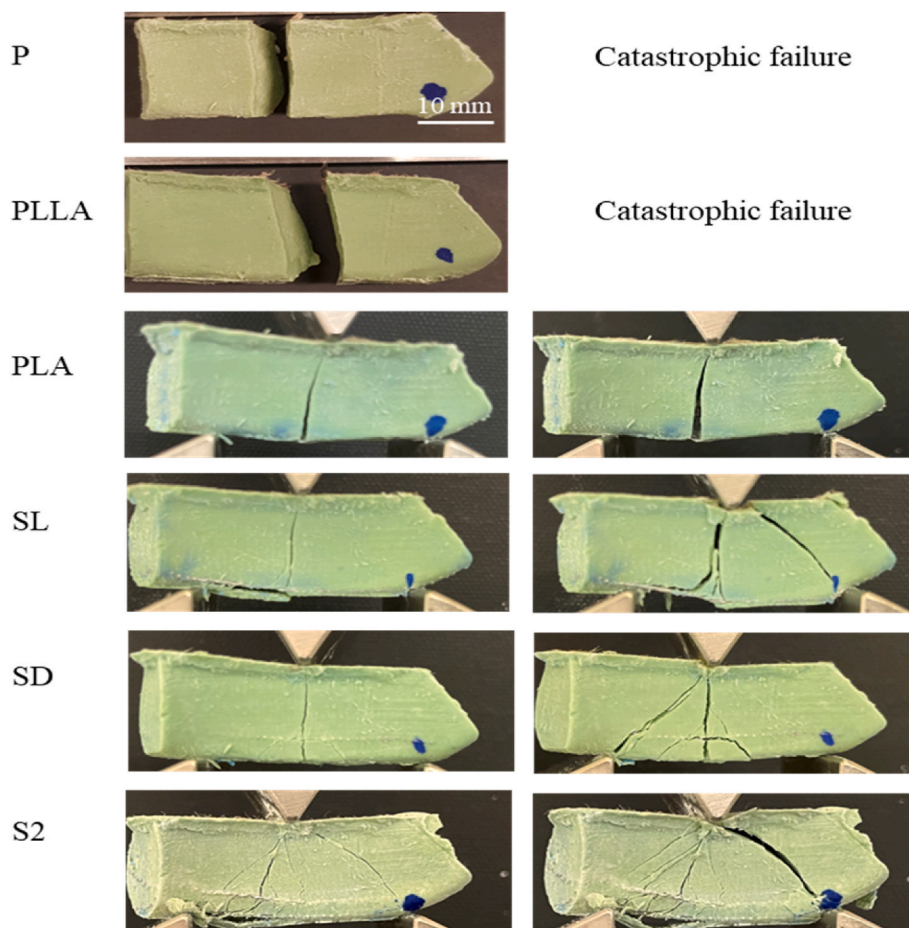


Fig. 6. snapshots of mandibular bone graft materials taken during the flexural tests.



Fig. 7. Snapshot of S2 sample loading in three-point bending showing the crack pattern, overlaid with the trajectories of principal tensile stresses.

than the first one. Small peaks and valleys on the load-deflection curve after the matrix fracture were due to the failure of the mesh fibers. Therefore, the failure mode of PLA was a flexure-shear failure. On the other hand, the PLLA mesh with a lower volume fraction and a low stiffness could not bridge the crack and prevent its growth. As a result, the mode of failure of PLLA was a catastrophic fracture, similar to that of P. For these samples, the failure was governed by flexural moment (Lin et al., 2021). Due to the abrupt fracture of these samples, taking snapshots during crack propagation was not possible. The lower peak load produced by PLA compared to PLLA can be attributed to differences in mesh geometry and the volume fraction of the mesh in these samples. In PLA, a higher amount of stiff CS is replaced by the reinforcement, leading to lower resistance to external loads. Moreover, the mesh may act as a stress concentrator in the brittle matrix (Tuan and Chen, 2002),

accelerating failure. This effect is more pronounced in PLA due to the higher open area (44% for PLA vs 9% for PLLA) and higher volume fraction of the mesh. However, due to the higher volume fraction of the reinforcement in PLA, the sample could carry some load even after initial crack propagation. Our experimental observations showed that the adhesion of polymeric mesh to CS was weaker than that of metallic mesh to CS. As a result, interfacial crack propagation was more pronounced in PLA, while also present in PLLA.

Three mechanical properties can be obtained from the load-deflection curves: the maximum force each sample withstood under bending, stiffness, and the dissipated energy, which is defined as the

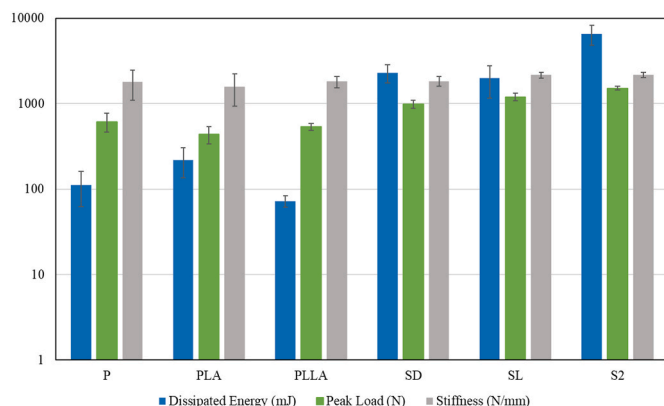


Fig. 8. Dissipated energy, stiffness, and maximum load in the reference material (P = plain CS), together with results from the reinforced bone grafts.

area under the force-displacement curve. Fig. 8 shows an overview of these properties for the various designs tested in this study. The incorporation of one layer of metallic mesh improved the mechanical performance of plain CS, so that SL and SD exhibited higher maximum loads, stiffness, and energy dissipation in comparison to P. However, in the case of one layer of metallic mesh, there was a trade-off between the maximum load, stiffness, and energy dissipation of SL and SD; hence the SL samples were stronger by 21.3% ($p < 0.05$), and stiffer by 17% ($p > 0.05$), while the SD samples dissipated higher amounts of energy by 16% ($p > 0.05$). Additionally, the increase in the number and volume fraction of the metallic reinforcement resulted in an even higher rise in dissipated energy, peak load, and stiffness; the highest dissipated energy, stiffness, and peak load were therefore found in the S2 samples. The improvements in the maximum load were 145.6%, 94.7%, and 60.40%, respectively, for S2, SL, and SD in comparison to P, while the energy dissipated by these samples respectively improved by 5767.85%, 1669.58%, and 1952.52%. These results were statically significant (p values < 0.05). The stiffness of SD, SL, and S2 was greater than that of P by respectively 3%, 21.3, and 21.9% (p values > 0.05). In the case of polymeric reinforcement, while PLLA had a detrimental effect on both dissipated energy by 35.31% and peak load by 13.05%, PLA dissipated 96.71% more energy despite its adverse effect by 29.18% on the peak load. However, these results were not statistically significant (p values > 0.05). While the stiffness of PLLA was marginally higher than P by 1.6%, PLA showed a lower stiffness by 11% (p values > 0.05).

The objective of this work was to produce a patient-specific bone graft material with properties that approach those of natural bone. However, comparing the peak load, dissipated energy, and stiffness values is challenging, as these are geometry-dependent properties. We previously tested the properties of CS grafts reinforced with different numbers of layers, titanium volume fractions, and open area, using regular beams that allowed for the calculations of stresses and strains (Cavelier et al., 2021). These materials displayed flexural strength, elastic modulus, and toughness respectively in the range of 12–54 MPa, 1.6–18.6 GPa, and 0.06–12 MJ/m³. In comparison, the flexural strength of cortical bone ranges from 103 to 300 MPa (Thangavel and ElsenSelvam, 2022; Keller et al., 1990; Roohani-Esfahani et al., 2016; Martínez-Vázquez et al., 2014), and the strength of cancellous (trabecular) bone is in the 10–25 MPa range (Thangavel and ElsenSelvam, 2022; Roohani-Esfahani et al., 2016). The toughness of our CS-based bone graft materials, however, surpasses that of cortical bone, 0.5–1 MJ/m³ (Martínez-Vázquez et al., 2014). These materials also displayed an elastic modulus within the range of cortical bone modulus 7–30 GPa (Keller et al., 1990; Eqtessadi et al., 2016).

6. Conclusions

We developed bioinspired load-bearing bone graft materials that can be customized to complex, patient-specific geometries. The tight control over the architecture of the material offered by this protocol enables the designing of bone graft materials inspired by the architecture of the mandible to maximize several competing properties, such as strength and toughness (Ritchie, 2011). We evaluated the geometry fidelity of our method through a quantitative comparison of two bone graft materials replicating the shapes of the orbital floor and lateral orbital rim. We also studied the mechanical properties and fracture behavior of bone graft materials replicating the geometry of the mandible body with six different design configurations. Our findings attested the following.

- The method could replicate the complex geometry of facial bones with high accuracy, achieving deviations within the range of –1.03 to 1.6 mm for the orbital floor and –1.25 to 0.97 mm for the lateral orbital rim.
- The presence of powerful toughening mechanisms such as crack deflection, crack bridging, and multiple cracking resulting from

metal mesh reinforcement was crucial for overcoming brittleness through crack control and achieving high mechanical performance.

- For a given volume fraction of reinforcement, high peak loads and stiffness were achieved by placing the metal mesh at the lowermost margin of the samples, while high energy dissipation was achieved by embedding the mesh within the mandibular samples. However, S2 samples exhibited the highest performance among all samples.
- The type of reinforcement used in the CS matrix had a profound effect on failure mode. The metallic mesh-reinforced CS failed due to a combination of shear, compression, and flexural failures. The failure mode of PLA was a flexure-shear failure. The failure mechanism of plain CS and PLLA was a flexural failure.
- Metallic mesh-reinforced samples showed more effective mechanical performance than polymeric mesh-reinforced samples by significantly improving both peak load and toughness. In contrast, PLA mesh-reinforced samples showed enhanced toughness but at the cost of peak load compared to plain CS. Reinforcement with PLLA mesh led to a decrease in both peak load and toughness compared to pure CS.

The multilayered bone graft materials inspired by the architecture of the mandible showed attractive mechanical performance which can be considered a promising step towards designing inexpensive bioresorbable and biocompatible materials for load-bearing applications. More specifically, we combined the strategy of reinforcing the mineral matrix with 3D printing to produce rapid and inexpensive patient-specific mesh/ceramic bone graft materials, benefiting from two powerful performance-enhancing strategies: forming the materials into multilayered structures and incorporation of a polymer/metal phase into the ceramic. These bone grafts can be reinforced with different arrangements of meshes which are made of distinct materials and architectures, allowing for regulating the properties to suit specific applications.

Furthermore, our bone grafts can be produced rapidly and at room temperature, unlike other bioceramics such as calcium phosphate which require lengthy and expensive sintering steps at elevated temperatures (Goel et al., 2013). Proteins, therapeutic drugs, and growth elements can potentially be incorporated into the bone graft materials. Autoclaving is not an appropriate sterilization method for CS because it can break down the material. Other approaches such as gamma radiation are however feasible to sterilize these bone graft materials (Frame, 1975). The three-point bending test provides valuable insights into the initial mechanical properties of the bone graft materials. However, since the mandible is a movable, load-bearing facial bone, complementary tests such as the FDA-recommended F382 fatigue tests are crucial to evaluate the long-term performance of the bone grafts under cyclic stresses. These tests together provide a thorough assessment of the mechanical behaviour of the bone grafts. Fatigue tests should however be interpreted in the context of the resorbability of the bone graft: A bioresorbable material may be replaced by natural bone after implantation, possibly before the material reaches its fatigue life (Bohner et al., 2012).

The medical method presented in this work can help reconstructive orthopedic surgeons ease their work, and increase patient success rates and quality of life by eliminating the need to harvest bone from donor sites and provide reliable materials.

CRedit authorship contribution statement

Seyed Alireza Mirmohammadi: Writing – review & editing, Writing – original draft, Visualization, Methodology, Investigation, Formal analysis, Conceptualization. **Damiano Pasini:** Writing – review & editing, Supervision, Resources, Funding acquisition. **Francois Barthelet:** Writing – review & editing, Supervision, Resources, Methodology, Funding acquisition, Conceptualization.

Declaration of competing interest

The authors declare that they have no known competing financial interests or personal relationships that could have appeared to influence the work reported in this paper.

Acknowledgments

This project was supported by a Collaborative Health Research Projects grant from CIHR and NSERC. SAM was partially supported by a McGill Engineering Doctoral Award from the Faculty of Engineering at McGill University.

Data availability

Data will be made available on request.

References

- Abar, B., et al., 2022. Outcomes of surgical reconstruction using custom 3D-printed porous titanium implants for critical-sized bone defects of the foot and ankle. *Foot Ankle Int.* 43 (6), 750–761.
- Abed, F., El-Chabib, H., AlHamaydeh, M., 2012. Shear characteristics of GFRP-reinforced concrete deep beams without web reinforcement. *J. Reinforc. Plast. Compos.* 31 (16), 1063–1073.
- Afroz, P.N., Bykowski, M.R., James, I.B., Daniali, L.N., Clavijo-Alvarez, J.A., 2015. The epidemiology of mandibular fractures in the United States, part 1: a review of 13,142 cases from the US National Trauma Data Bank. *J. Oral Maxillofac. Surg.* 73 (12), 2361–2366.
- Ansari, M.A.A., Jain, P.K., Nanda, H.S., 2023. Preparation of 3D printed calcium sulfate filled PLA scaffolds with improved mechanical and degradation properties. *Journal of Biomaterials Science* 34 (10), 1408–1429. *Polymer Edition*.
- Arabnejad, S., Johnston, B., Tanzer, M., Pasini, D., 2017. Fully porous 3D printed titanium femoral stem to reduce stress-shielding following total hip arthroplasty. *J. Orthop. Res.* 35 (8), 1774–1783. <https://doi.org/10.1002/jor.23445>.
- Asadi-Eyvdivand, M., Solati-Hashjin, M., Farzad, A., Osman, N.A.A., 2016. Effect of technical parameters on porous structure and strength of 3D printed calcium sulfate prototypes. *Robot. Comput. Integrated Manuf.* 37, 57–67.
- Bachelet, J.-T., Cordier, G., Porcheray, M., Bourlet, J., Gleizal, A., Foletti, J.-M., 2018. Orbital reconstruction by patient-specific implant printed in porous titanium: a retrospective case series of 12 patients. *J. Oral Maxillofac. Surg.* 76 (10), 2161–2167.
- Barthelat, F., 2015. Architecture materials in engineering and biology: fabrication, structure, mechanics and performance. *Int. Mater. Rev.* 60 (8), 413–430.
- Barthelat, F., Yin, Z., Buehler, M.J., 2016. Structure and mechanics of interfaces in biological materials. *Nat. Rev. Mater.* 1 (4), 1–16.
- Bohner, M., Galea, L., Doebelin, N., 2012. Calcium phosphate bone graft substitutes: failures and hopes. *J. Eur. Ceram. Soc.* 32 (11), 2663–2671.
- Campbell, G.H., Rühle, M., Dalgleish, B.J., Evans, A.G., 1990. Whisker toughening: a comparison between aluminum oxide and silicon nitride toughened with silicon carbide. *J. Am. Ceram. Soc.* 73 (3), 521–530.
- Canal, C., Ginebra, M., 2011. Fibre-reinforced calcium phosphate cements: a review. *J. Mech. Behav. Biomed. Mater.* 4 (8), 1658–1671.
- Carmona, J.R., Ruiz, G., del Viso, J.R., 2007. Mixed-mode crack propagation through reinforced concrete. *Eng. Fract. Mech.* 74 (17), 2788–2809.
- Castro, A.G., et al., 2017. Incorporation of PLLA micro-fillers for mechanical reinforcement of calcium-phosphate cement. *J. Mech. Behav. Biomed. Mater.* 71, 286–294.
- Cavelier, S., Dastjerdi, A.K., McKee, M.D., Barthelat, F., 2018. Bone toughness at the molecular scale: a model for fracture toughness using crosslinked osteopontin on synthetic and biogenic mineral substrates. *Bone* 110, 304–311. <https://doi.org/10.1016/j.bone.2018.02.022>.
- Cavelier, S., Tanzer, M., Barthelat, F., 2020. Maximizing the strength of calcium sulfate for structural bone grafts. *J. Biomed. Mater.* 108 (4), 963–971.
- Cavelier, S., Mirmohammadi, S., Barthelat, F., 2021. Titanium mesh-reinforced calcium sulfate for structural bone grafts. *J. Mech. Behav. Biomed. Mater.* 118, 104461.
- Chen, Z., Mecholsky Jr., J.J., 1993. Toughening by metallic lamina in nickel/alumina composites. *J. Am. Ceram. Soc.* 76 (5), 1258–1264.
- Chen, W.-C., et al., 2017. A comparison of the heat treatment duration and the multilayered effects on the poly (lactic) acid braid reinforced calcium phosphate cements used as bone tissue engineering scaffold. *J. Ind. Textil.* 46 (8), 1668–1683.
- Clegg, W., Kendall, K., Alford, N.M., Button, T., Birchall, J., 1990. A simple way to make tough ceramics. *Nature* 347 (6292), 455–457.
- Deliormanli, A.M., Rahaman, M.N., 2012. Direct-write assembly of silicate and borate bioactive glass scaffolds for bone repair. *J. Eur. Ceram. Soc.* 32 (14), 3637–3646.
- Demir, A., Caglar, N., Ozturk, H., 2019. Parameters affecting diagonal cracking behavior of reinforced concrete deep beams. *Eng. Struct.* 184, 217–231.
- Dérand III, P., Rännar, L.-E., Hirsch, J.-M., 2012. Imaging, virtual planning, design, and production of patient-specific implants and clinical validation in craniomaxillofacial surgery. *Craniomaxillofacial Trauma Reconstr.* 5 (3), 137–143.
- DeStefano, V., Khan, S., Tabada, A., 2020. Applications of PLA in modern medicine. *Engineered Regeneration* 1, 76–87.
- Dienel, K., et al., 2022. Patient-specific bioimplants and reconstruction plates for mandibular defects: production workflow and in vivo large animal model study. *Macromol. Biosci.* 22 (4), 2100398.
- Du, S., et al., 2024. Bioactive polymer composite scaffolds fabricated from 3D printed negative molds enable bone formation and vascularization. *Acta Biomater.*
- Eqtesadi, S., Motealleh, A., Pajares, A., Guiberteau, F., Miranda, P., 2016. Improving mechanical properties of 13–93 bioactive glass robocast scaffold by poly (lactic acid) and poly (ϵ -caprolactone) melt infiltration. *J. Non-Cryst. Solids* 432, 111–119.
- Esslinger, S., Gadow, R., 2020. Additive manufacturing of bioceramic scaffolds by combination of FDM and slip casting. *J. Eur. Ceram. Soc.* 40 (11), 3707–3713.
- Evans, A.G., 1990. Perspective on the development of high-toughness ceramics. *J. Am. Ceram. Soc.* 73 (2), 187–206.
- Evans, A.G., He, M.Y., Hutchinson, J.W., 1989. Interface debonding and fiber cracking in brittle matrix composites. *J. Am. Ceram. Soc.* 72 (12), 2300–2303.
- Falkhausen, R., Mitsimponas, K., Adler, W., Brand, M., von Wilmsowky, C., 2021. Clinical outcome of patients with orbital fractures treated with patient specific CAD/CAM ceramic implants—a retrospective study. *J. Cranio-Maxillofacial Surg.* 49 (6), 468–479.
- Frame, J., 1975. Porous calcium sulphate dihydrate as a biodegradable implant in bone. *J. Dent.* 3 (4), 177–187.
- Fu, Q., Saiz, E., Tomsia, A.P., 2011. Direct ink writing of highly porous and strong glass scaffolds for load-bearing bone defects repair and regeneration. *Acta Biomater.* 7 (10), 3547–3554.
- Goel, S.C., Singh, D., Rastogi, A., Kumaraswamy, V., Gupta, A., Sharma, N., 2013. Role of Tricalcium Phosphate Implant in Bridging the Large Osteoperiosteal Gaps in Rabbits. *GrabCAD*, 2018. <https://grabcad.com/library/skull-43> (accessed November 2022).
- Hamano, R., Nakagawa, Y., Irawan, V., Ikoma, T., 2021. Mechanical anisotropy and fracture mode of binder jetting 3D printed calcium sulfate moldings. *Appl. Mater. Today* 25, 101160.
- Hasan, M.S., Carpenter, N., Wei, T.L., McNally, D., Ahmed, I., Boszczyk, B.M., 2014. Effects of adding resorbable phosphate glass fibres and PLA to calcium phosphate bone cements. *J. Appl. Biomater. Funct. Mater.* 12 (3), 203–209.
- Honigmann, P., Sharma, N., Okolo, B., Popp, U., Msallem, B., Thieringer, F.M., 2018. Patient-specific surgical implants made of 3D printed PEEK: material, technology, and scope of surgical application. *BioMed Res. Int.* 2018 (1), 4520636.
- Howard, S., Pateras, S., Clyne, T., 1998. Effect of interfacial adhesion on toughness of metal/ceramic laminates. *Mater. Sci. Technol.* 14 (6), 535–541.
- Hu, J., Wang, J.H., Wang, R., Yu, X.B., Liu, Y., Baur, D.A., 2019. Analysis of biomechanical behavior of 3D printed mandibular graft with porous scaffold structure designed by topological optimization. *3D Printing in Medicine* 5, 1–14.
- Ivanovski, S., Staples, R., Arora, H., Vaquette, C., Alayan, J., 2024. Alveolar Bone Regeneration Using a 3D-printed Patient-specific Resorbable Scaffold for Dental Implant Placement: A Case Report. *Clinical Oral Implants Research*.
- Jain, R., et al., 2021. Feasibility of customised polymethyl methacrylate implants fabricated using 3D printed flexible moulds for correction of facial skeletal deformities. *J. Craniofac. Surg.* 32 (6), 1981–1985.
- Keller, T., Mao, Z., Spengler, D., 1990. Young's modulus, bending strength, and tissue physical properties of human compact bone. *J. Orthop. Res.* 8 (4), 592–603.
- Kim, N.-h., et al., 2024. Customized three-dimensional printed ceramic bone grafts for osseous defects: a prospective randomized study. *Sci. Rep.* 14 (1), 3397.
- Klammert, U., Gbureck, U., Vorndran, E., Rödiger, J., Meyer-Marcotty, P., Kübler, A.C., 2010. 3D powder printed calcium phosphate implants for reconstruction of cranial and maxillofacial defects. *J. Cranio-Maxillofacial Surg.* 38 (8), 565–570.
- Krstic, V.D., 1983. On the fracture of brittle-matrix/ductile-particle composites. *Philos. Mag.* 48 (5), 695–708.
- Launey, M.E., Buehler, M.J., Ritchie, R.O., 2010. On the mechanistic origins of toughness in bone. *Annu. Rev. Mater. Res.* 40, 25–53.
- Laurencin, C.T., Khan, Y., Veronick, J., 2014. "bone graft substitutes: past, present, and future." In: *Bone Graft Substitutes and Bone Regenerative Engineering*. ASTM International, pp. 1–9.
- Lethaus, B., Bloebaum, M., Koper, D., Poort-ter Laak, M., Kessler, P., 2014. Interval cranioplasty with patient-specific implants and autogenous bone grafts—success and cost analysis. *J. Cranio-Maxillofacial Surg.* 42 (8), 1948–1951.
- Lin, Y., Yan, J., Wang, Z., Fan, F., Zou, C., 2021. Ultimate capacity and failure mechanism of SCS and S-UHPC composite deep beams: test and modeling. *Eng. Struct.* 245, 112874.
- Ma, H., Feng, C., Chang, J., Wu, C., 2018. 3D-printed bioceramic scaffolds: from bone tissue engineering to tumor therapy. *Acta Biomater.* 79, 37–59.
- MacGregor, J.G., Wight, J.K., Teng, S., Irawan, P., 1997. *Reinforced Concrete: Mechanics and Design*. Prentice Hall, Upper Saddle River, NJ.
- Martínez-Vázquez, F.J., Pajares, A., Guiberteau, F., Miranda, P., 2014. Effect of polymer infiltration on the flexural behavior of β -tricalcium phosphate robocast scaffolds. *Materials* 7 (5), 4001–4018.
- Masaeli, R., Zandsalimi, K., Rasoulboroujeni, M., Tayebi, L., 2019. Challenges in three-dimensional printing of bone substitutes. *Tissue Eng., Part B* 25 (5), 387–397.
- McCormac, J.C., Brown, R.H., 2015. *Design of Reinforced Concrete*. John Wiley & Sons.
- Mirkhalaf, M., et al., 2021a. Highly substituted calcium silicates 3D printed with complex architectures to produce stiff, strong and bioactive scaffolds for bone regeneration. *Appl. Mater. Today* 25, 101230.
- Mirkhalaf, M., Dao, A., Schindeler, A., Little, D.G., Dunstan, C.R., Zreiqat, H., 2021b. Personalized Baghdadite scaffolds: stereolithography, mechanics and in vivo testing. *Acta Biomater.* 132, 217–226.

- S. A. Mirmohammadi, D. Pasini, and F. Barthelat, "Controlling Strength and Dissolution in Calcium Sulfate Bone Graft Materials," unpublished results.
- Mirmohammadi, S.A., Pasini, D., Barthelat, F., 2022. Modeling, design and tailoring of a tough, strong and stiff multilayered bone graft material. *J. Mech. Behav. Biomed. Mater.* 134, 105369.
- Moiduddin, K., Mian, S.H., Umer, U., Alkhalefah, H., Ahmed, F., Hashmi, F.H., 2023. Design, analysis, and 3D printing of a patient-specific polyetheretherketone implant for the reconstruction of zygomatic deformities. *Polymers* 15 (4), 886.
- Moore, W.R., Graves, S.E., Bain, G.I., 2001. Synthetic bone graft substitutes. *ANZ J. Surg.* 71 (6), 354–361.
- Mulky, E., Yazgan, G., Maniura-Weber, K., Luginbuehl, R., Fortunato, G., Bühlmann-Popa, A.-M., 2014. Fabrication of biopolymer-based staple electrospun fibres for nanocomposite applications by particle-assisted low temperature ultrasonication. *Mater. Sci. Eng. C* 45, 277–286.
- Paré, A., et al., 2022. Standardized and axially vascularized calcium phosphate-based implants for segmental mandibular defects: a promising proof of concept. *Acta Biomater.* 154, 626–640.
- Petre, D.-G., Kucko, N.W., Abbadessa, A., Vermonden, T., Polini, A., Leeuwenburgh, S.C., 2019. Surface functionalization of polylactic acid fibers with alendronate groups does not improve the mechanical properties of fiber-reinforced calcium phosphate cements. *J. Mech. Behav. Biomed. Mater.* 90, 472–483.
- Pietrzak, W.S., Ronk, R., 2000. Calcium sulfate bone void filler: a review and a look ahead. *J. Craniofac. Surg.* 11 (4), 327–333.
- Qi, X., et al., 2017. Three dimensional printing of calcium sulfate and mesoporous bioactive glass scaffolds for improving bone regeneration in vitro and in vivo. *Sci. Rep.* 7 (1), 42556.
- Ritchie, R.O., 2011. The conflicts between strength and toughness. *Nat. Mater.* 10 (11), 817–822.
- Roohani-Esfahani, S.-I., Newman, P., Zreiqat, H., 2016. Design and fabrication of 3D printed scaffolds with a mechanical strength comparable to cortical bone to repair large bone defects. *Sci. Rep.* 6 (1), 19468.
- Rudman, K., Hoekzema, C., Rhee, J., 2011. Computer-assisted innovations in craniofacial surgery. *Facial Plast. Surg.* 27 (4), 358–365.
- Rühle, M., Evans, A.G., 1989. High toughness ceramics and ceramic composites. *Prog. Mater. Sci.* 33 (2), 85–167.
- Sapkal, P.S., Kuthe, A.M., Kashyap, R.S., Nayak, A.R., Kuthe, S.A., Kawle, A.P., 2017. Indirect casting of patient-specific tricalcium phosphate zirconia scaffolds for bone tissue regeneration using rapid prototyping methodology. *J. Porous Mater.* 24, 1013–1023.
- Sayyad, A.S., Patankar, S.V., 2013. Effect of stirrups orientation on flexural response of RC deep beams. *Am. J. Civ. Eng. Architect.* 1 (5), 107–111.
- Schumacher, M., Deisinger, U., Detsch, R., Ziegler, G., 2010. Indirect rapid prototyping of biphasic calcium phosphate scaffolds as bone substitutes: influence of phase composition, macroporosity and pore geometry on mechanical properties. *J. Mater. Sci. Mater. Med.* 21, 3119–3127.
- Shao, H., et al., 2018. Custom repair of mandibular bone defects with 3D printed bioceramic scaffolds. *J. Dent. Res.* 97 (1), 68–76.
- Shaw, M., Marshall, D., Dadkhah, M., Evans, A., 1993. Cracking and damage mechanisms in ceramic/metal multilayers. *Acta Metall. Mater.* 41 (11), 3311–3322.
- Smith, J.A., Petersmann, S., Arbeiter, F., Schäfer, U., 2023. Optimization and manufacture of polyetheretherketone patient specific cranial implants by material extrusion—A clinical perspective. *J. Mech. Behav. Biomed. Mater.*, 105965
- Tennyson, M., Krzak, A.M., Krkovic, M., Abdulkarim, A., 2021. Cambridge protocol for management of segmental bone loss. *J. Orthop. Case Rep.* 11 (1), 45.
- Tesavibul, P., et al., 2012. Processing of 45S5 Bioglass® by lithography-based additive manufacturing. *Mater. Lett.* 74, 81–84.
- Thangavel, M., Elsen Selvam, R., 2022. Review of physical, mechanical, and biological characteristics of 3D-printed bioceramic scaffolds for bone tissue engineering applications. *ACS Biomater. Sci. Eng.* 8 (12), 5060–5093.
- Thomas, N.R., 2013. Influence of Porcine Dermal Fibers and PLLA Fibers on Properties of a Commercially-Available Injectable Bone Graft Substitute.
- Thomas, M.V., Puleo, D.A., 2009. Calcium sulfate: properties and clinical applications. *J. Biomed. Mater. Res. B Appl. Biomater.* 88 (2), 597–610.
- Thouless, M.D., Evans, A.G., 1988. Effects of pull-out on the mechanical properties of ceramic-matrix composites. *Acta Metall.* 36 (3), 517–522.
- Topoleski, L.D.T., Ducheyne, P., Cuckler, J.M., 1992. The fracture toughness of titanium-fiber-reinforced bone cement. *J. Biomed. Mater. Res.* 26 (12), 1599–1617. <https://doi.org/10.1002/jbm.820261206>.
- Tuan, W.-H., Chen, R.-Z., 2002. Interactions between toughening mechanisms: transformation toughening versus plastic deformation. *J. Mater. Res.* 17 (11), 2921–2928.
- van Eijden, T., 2000. Biomechanics of the mandible. *Crit. Rev. Oral Biol. Med.* 11 (1), 123–136.
- Van Damme, L., Briant, E., Blondeel, P., Van Vlierberghe, S., 2020. Indirect versus direct 3D printing of hydrogel scaffolds for adipose tissue regeneration. *Mrs Advances* 5 (17), 855–864.
- Wang, W., Yeung, K.W., 2017. Bone grafts and biomaterials substitutes for bone defect repair: a review. *Bioact. Mater.* 2 (4), 224–247.
- Wang, J.-Q., Jiang, B.-J., Guo, W.-J., Zhao, Y.-M., 2019. Indirect 3D printing technology for the fabrication of customised β -TCP/chitosan scaffold with the shape of rabbit radial head—an in vitro study. *J. Orthop. Surg. Res.* 14 (1), 1–9.
- Wang, S., et al., 2021. Multiplied bending ductility and toughness of titanium matrix composites by laminated structure manipulation. *Mater. Des.* 197, 109237.
- Weir, M.D., Xu, H.H., Simon Jr., C.G., 2006. Strong calcium phosphate cement-chitosan-mesh construct containing cell-encapsulating hydrogel beads for bone tissue engineering. *J. Biomed. Mater. Res.* 77 (3), 487–496.
- Wong, R.C., Tideman, H., Kin, L., Merckx, M.A., 2010. Biomechanics of mandibular reconstruction: a review. *Int. J. Oral Maxillofac. Surg.* 39 (4), 313–319.
- Xiao, L., Abbaschian, R., 1992. Role of matrix/reinforcement interfaces in the fracture toughness of brittle materials toughened by ductile reinforcements. *Metall. Trans. A* 23, 2863–2872.
- Xu, H.H., Simon Jr., C.G., 2004. Self-hardening calcium phosphate cement-mesh composite: reinforcement, macropores, and cell response. *J. Biomed. Mater. Res.* 69 (2), 267–278.
- Xu, H.H., Quinn, J.B., Takagi, S., Chow, L.C., 2004. Synergistic reinforcement of in situ hardening calcium phosphate composite scaffold for bone tissue engineering. *Biomaterials* 25 (6), 1029–1037.
- Yang, J.-M., Tieg, T., 1995. Strength and toughness of ceramic composites at elevated temperatures. In: *High Temperature Mechanical Behaviour of Ceramic Composites*. Butterworth-Heinemann, pp. 87–119.
- Yang, J.Z., Sultana, R., Hu, X.Z., Ichim, P., 2014. Novel layered hydroxyapatite/tricalcium phosphate-zirconia scaffold composite with high bending strength for load-bearing bone implant application. *Int. J. Appl. Ceram. Technol.* 11 (1), 22–30.
- Yao, Y., Qin, W., Xing, B., Sha, N., Jiao, T., Zhao, Z., 2021. High performance hydroxyapatite ceramics and a triply periodic minimum surface structure fabricated by digital light processing 3D printing. *Journal of Advanced Ceramics* 10, 39–48.
- Yuan, J., Cui, L., Zhang, W.J., Liu, W., Cao, Y., 2007. Repair of canine mandibular bone defects with bone marrow stromal cells and porous β -tricalcium phosphate. *Biomaterials* 28 (6), 1005–1013.
- Zhang, Z., Zhang, Y.-W., Gao, H., 2011. On optimal hierarchy of load-bearing biological materials. *Proc. Biol. Sci.* 278 (1705), 519–525.
- Zhang, F., et al., 2022. Digital light processing of β -tricalcium phosphate bioceramic scaffolds with controllable porous structures for patient specific craniomaxillofacial bone reconstruction. *Mater. Des.* 216, 110558.
- Zok, F., Hom, C., 1990. Large scale bridging in brittle matrix composites. *Acta Metall. Mater.* 38 (10), 1895–1904.
- Zuo, Y., Yang, F., Wolke, J.G., Li, Y., Jansen, J.A., 2010. Incorporation of biodegradable electrospun fibers into calcium phosphate cement for bone regeneration. *Acta Biomater.* 6 (4), 1238–1247.